*Article*

# Research on Fast Detection Technology of Dark Current in Ge-Si Detector Array

**Zhen Gao[1], Min Tao[1*], Xuetong Li[1], Junfeng Song[1,2], Zijian Liu[1], Ziming Wang[1] and Chengming Li[1]**

[1] State Key Laboratory of Integrated Optoelectronics, College of Electronic Science and Engineering, Jilin University, Changchun 130012, China
[2] Peng Cheng Laboratory, Shenzhen 518055, China
* Correspondence: taomin@jlu.edu.cn (M.T.)

**Abstract:** The shortwave infrared Ge-Si photodetector will become the core device of the LiDAR optical receiver. In order to meet the urgent demand for photodetectors in the LiDAR field, we have designed and produced a 32×32 pixel Ge-Si photodetector array proposed and developed to meet the performance requirements of the detector array. A dark current detection system for fast scanning and detecting large-scale Ge-Si detector arrays is proposed and developed to achieve rapid detection of dark current in each pixel of the detector. The system was used to validate the main performance indicators of the detector array we designed, achieving rapid discrimination of array performance and rapid localization of damaged pixels. The scanning test results show that the average dark current of the detector array chip we designed is at the nano ampere level, and the proportion of bad points is less than 1%. The consistency of the array chip is high, which can meet the requirements of light detection at the receiving end of the LiDAR. This work laid the foundation for our subsequent development of a LiDAR prototype system.

**Keywords:** short wave infrared; LiDAR; photodetector array; dark current detection

## 1. Introduction

The application of LiDAR is very extensive, and in the future, it will have a super large market worth hundreds of billions of yuan [1-3]. Lidar is a radar system that uses lasers to accurately measure the position, velocity, and other characteristics of targets. It is an optical remote sensing technology that can transmit distance information from the real world to computers, giving machines human depth vision and providing the function of "eyes" for humans to explore a wider three-dimensional world. LiDAR can be used for intelligent transportation, real-time monitoring of vehicle characteristics (size, speed, volume) and flow; Can be used for intelligent vehicles (intelligent connected vehicles), ranging and speed measurement, obstacle avoidance navigation; It can be used for intelligent robots to achieve precise positioning, gesture recognition, etc; Can be used for unmanned aerial vehicles for land surveying and environmental monitoring; Can be used for intelligent healthcare, achieving virtual imaging and 3D printing; Can be used for digital cities, urban 3D modeling, digital maps, etc. [4-9]. In the military, it can be used for battlefield reconnaissance, fighter telemetry, fire control tracking, underwater detection, laser communication, electronic countermeasures, and so on [10-13]. Short-wave infrared is safer for the human eye and is the best choice for LiDAR light sources. Short wave infrared generally refers to wavelengths between 0.9μm~1.7μm. The electromagnetic waves between 0.9μm~1.7μm cannot be seen by the human eye, but they are very similar to visible light and can be reflected on the surface of an object. The image has shadows and contrast, making the object easy to recognize. Short wave infrared technology has a series of outstanding advantages such as high recognition, all-weather adaptation, low light night vision, covert active imaging, and simple optical configuration, making it have special application prospects in fields such as aerospace remote sensing, archaeological identification, military reconnaissance, public safety, industrial testing, medical diagnosis, etc. [15-17].

At present, short infrared wavelength InGaAs avalanche photodiode detectors have started to be applied in high-end LiDAR, but the cost is relatively high [18]; Ge-Si photodetectors that are

Preprints (www.preprints.org) | NOT PEER-REVIEWED | Posted: 20 April 2023 doi:10.20944/preprints202304.0598.v1

compatible with CMOS technology and have lower costs have been extensively studied in the past decade, and have made remarkable progress [19-28]. Especially in the past year or two, research has shown that the performance of Ge avalanche photodiode single-photon detectors at low temperatures is comparable to that of InGaAs [19]. Moreover, from an integration perspective, making Ge photodetectors on single crystal Si is compatible with Si-based CMOS technology and can be integrated with integrated circuits and optical circuits on a single chip. With low cost and high integration, it will become the mainstream of LiDAR detectors. Therefore, the research on Ge-Si photodetectors has become increasingly important. Early Ge-Si photodetectors were mainly used in the field of optical communication, so more attention was paid to the Gain-bandwidth product and weak light detection limit. The Gain-bandwidth product has reached above 300GHz [20, 21]; The Si waveguide made by the Institute of Electronics at the University of Paris Soude on a 300nm Ge epitaxial layer is integrated with a Ge Si photodetector on a single chip. The weak light detection limit can be as low as -35dBm, while the bias voltage is only 7V [22]. The University of Herry Watt in the UK has conducted a series of research on single photon Ge-Si APD. In 2013, they produced a traditional vertical structure Ge-Si APD, which achieved a single photon detection function in the Geiger mode at a low temperature of 100K[23]; The Sandia National Laboratory in the United States has produced a novel horizontal structure Ge-Si APD, which improves the single photon detection efficiency to 5.27%, providing a strong technical foundation for the implementation of ultra-long range LiDAR [24]. The Singapore Institute of Microelectronics first reported the research results of Ge-Si APD arrays forming photomultiplier tubes at the 2019 OFC International Conference [25], and the photoelectric detection efficiency between array units showed good consistency. But the dark current is still relatively high, and the dark current near the breakdown voltage of the single transistor APD also reaches μA-level. Academician Wang Qiming's research group at the Institute of Semiconductors of the Chinese Academy of Sciences has studied the epitaxial growth of Ge on monocrystalline silicon using ultra-high vacuum CVD. Recently, extensive research has been conducted on Ge-Sn alloys [26]. Xiamen University has studied upper and lower DBR microcavity-enhanced germanium photodetectors with similar surface emission structures [27], but the photoelectric conversion efficiency is slightly low; The Zhiping Zhou research group at Peking University studied a short cavity Ge-Si photodetector with enhanced horizontal DBR reflection 5μm. The long absorption region achieves a photoelectric conversion efficiency of 0.72A/W, while the 3dB bandwidth reaches 31.7GHz, while the dark current is only 7nA [28].

In response to the urgent demand for photodetectors in the field of LiDAR, we have conducted research on PIN-type Ge-Si photodetectors. By optimizing the doping structure and concentration design, we have effectively suppressed the electric field distributed at Ge and Si heterojunctions and prepared low dark current and high responsiveness 32×32 pixel Ge-Si photodetector array. In order to test the performance of the detector array, we designed a fast dark current detection system. The system quickly scans each pixel of the array, applies different bias voltages to each pixel, and reads the different dark currents generated by the pixel. Based on the characteristic that the dark current of the detector is inversely proportional to its optical response characteristics, the performance of the detector is judged by comparing the magnitude of the dark current. This system can quickly detect the dark current distribution of the entire array and locate damaged pixels, providing us with testing and verification methods for device design. It can be used for the rapid detection of dark current in larger detector arrays in the future.

## 2. Principle and System

### *2.1. New Ge-Si detector array*

A photodetector is a device that converts light signals into electrical signals. In order to effectively capture the reflected light signals of the target object on the LiDAR in space, we designed and prepared a 32×32 pixel area array Ge-Si photodetector array with a Ge active area of up to 707μm$^2$, as shown in Figure 1. The array consists of pixels, leads, and electrodes. The doping structure of pixels is achieved by injecting boron elements into the top Si layer on the SOI wafer, forming a P-

Preprints (www.preprints.org) | NOT PEER-REVIEWED | Posted: 20 April 2023 doi:10.20944/preprints202304.0598.v1

type doping region and a heavily doped P++ region, respectively. The P++ region forms a cathode through ohmic contact with the Al metal electrode. Afterwards, selective epitaxy was carried out on Si substrate to prepare Ge thin films as the active absorption region of the detector. Finally, phosphorus element is injected above the Ge absorption region to form a heavily doped N++ region, which forms an anode through ohmic contact with the Al electrode.

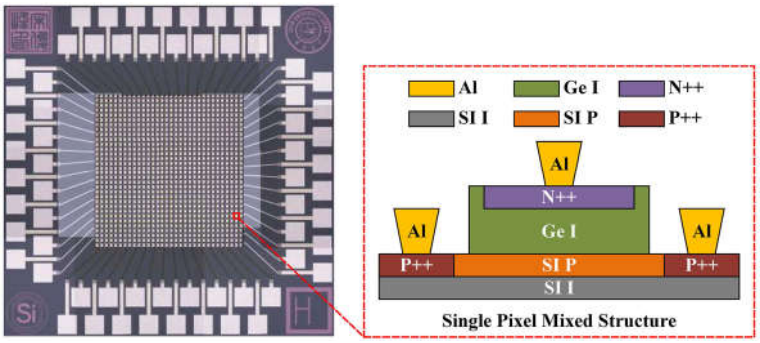


**Figure 1.** New Ge-Si detector array structure.

In order to characterize the characteristics of photodetectors, we mainly study their responsivity and quantum efficiency, dark current, noise characteristics, response bandwidth, gain, Gain-bandwidth product, and other parameters [29]. When the photodetector is in a reverse bias state, even without incident light, a weak current is generated, known as a dark current. The generation of dark current is related to the electron-hole pairs generated by the thermal motion inside the detector on the one hand; On the other hand, it is related to the defect of the detector surface, bias voltage, and surface area. Figure 2(a) shows the equivalent circuit model of the PIN photodetector under no light conditions. In the circuit, $C_j$ is the junction capacitance, $C_s$ is the equivalent parallel capacitance, $R_s$ is the equivalent series resistance, and the dark current $I_{dark}$ includes reverse bias current $I_{gen}$, tunneling current $I_{tun}$, and parasitic leakage current $I_{ohm}$ [30]. Figure 2(b) shows the corresponding bias voltage dark current curve, where the dark current increases with the increase of the reverse bias voltage.

As shown in Equation 1, the dark current can be expressed as:

$$I_{dark} = I_{gen} + I_{tun} + I_{ohm} \tag{1}$$

Under reverse bias voltage, electron-hole pairs are generated in the space charge region. Once an electron hole is generated, it is swept out of the space charge region by an electric field, forming a reverse bias to generate current. Equation 2 is the calculation method for the current $I_{gen}$ generated by reverse bias:

$$I_{gen} = \frac{Aen_i w}{2\tau_0} \tag{2}$$

Among them, $\tau_0$ is the average lifetime of the carrier, $n_i$ is the intrinsic carrier concentration, $e$ is the electron charge, $w$ is the volume of the space charge region, and $A$ is the device area.

According to the tunneling effect, when the reverse bias voltage is too high, the probability of carriers passing through the barrier width of the space charge region greatly increases, resulting in a large current that cannot be ignored. This current is called tunneling current, and the calculation method for tunneling current is:

$$I_{tun} = \left(\frac{2m^*}{E_g}\right)^{\frac{1}{2}} \cdot \exp\left(-\frac{4}{3eE\hbar}\sqrt{2m^* E_g^3}\right) \cdot A \cdot \frac{e^3 EV}{4\pi^2 \hbar^2} \tag{3}$$

Where $E$ is the maximum field strength in the depletion region of the PN junction, $V$ is the applied reverse bias voltage, $A$ is the device area, $m^*$ is the effective mass of the electron, $E_g$ is the energy band gap, and e is the electronic quantity.

Preprints (www.preprints.org) | NOT PEER-REVIEWED | Posted: 20 April 2023 doi:10.20944/preprints202304.0598.v1

The expression for parasitic leakage current is:

$$I_{ohm} = \frac{V}{R_d} \tag{4}$$

Among them, $V$ is the bias voltage applied at both ends of the detector, and $R_d$ is the dark resistance of the photodetector. Generally speaking, the dark current mainly generates current and parasitic leakage current at low bias, and tunneling current at high bias. Therefore, it is necessary to check the distribution of dark current under different reverse bias voltages, and to improve the performance of photodetectors, efforts should be made to reduce dark current.

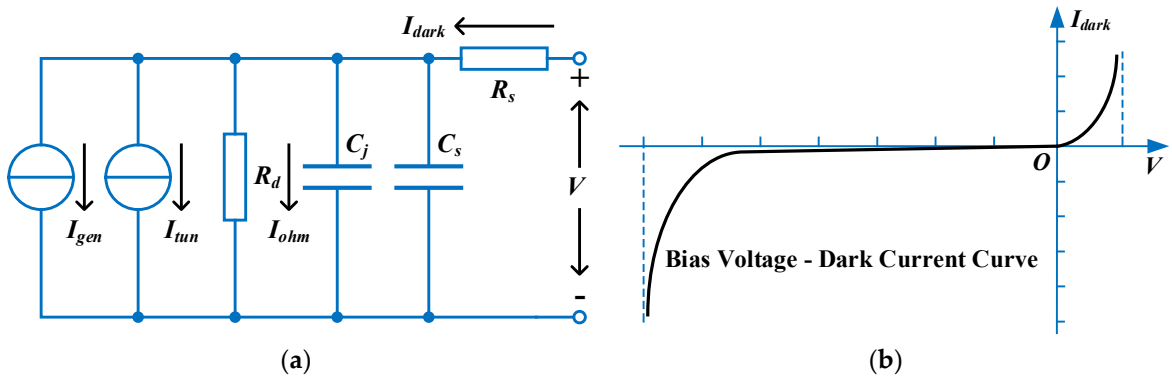


**Figure 2.** PIN photodetector circuit model and dark current curve. (**a**) PIN equivalent circuit model under no illumination. (**b**) Bias voltage dark current curve.

*2.2. Scanning detection method and system*

Figure 3 is the principle block diagram of the germanium silicon detector array dark current fast detection system, which consists of a controllable voltage source, a Ge-Si detector array and its scanning circuit, an electrometer level amplifier, a programmable amplifier, an MCU (micro-controller) and an LCD (liquid crystal display). During the working process, the MCU controls the bipolar DAC (digital-to-analog converter) output voltage in the controllable voltage source, which is amplified by a voltage follower to generate a controllable bias voltage. The controllable bias voltage is loaded onto the optical relay. The MCU controls the 3-8 decoder for row selection, selecting one row of pixels to make one row of pixels conductive. The MCU also controls the 3-8 decoder for column selection, selecting one column of pixels to make one column of pixels conductive, Finally, the bias voltage is applied to a single detector; The dark current signal generated by the pixel generates a voltage signal through the electrometer amplifier. The generated voltage signal is amplified by the programmable amplifier. The amplified voltage signal is input to the ADC (analog-to-digital converter) module in the MCU and converted into a digital signal, which is finally displayed on the LCD display screen. This system can achieve rapid scanning and dark current detection of large-scale Ge-Si detector arrays.

Preprints (www.preprints.org) | NOT PEER-REVIEWED | Posted: 20 April 2023 doi:10.20944/preprints202304.0598.v1

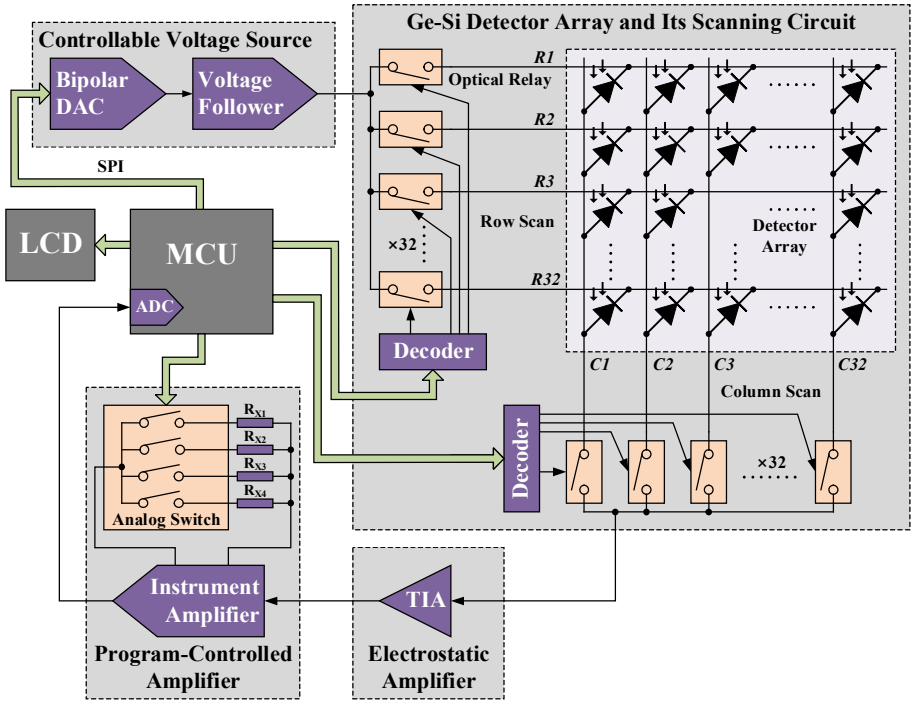


**Figure 3.** Schematic diagram of the composition of the detection system.

The controllable voltage source consists of a bipolar DAC and a voltage follower, with a bipolar DAC power supply voltage of ± 5V. Therefore, the bias voltage range of the detector can reach -5V to+5V. We continuously read the dark current under reverse bias voltage and also read the dark current under positive bias voltage. The actual voltage scanning range is -3V~+1V. As shown in Figure 4, the bipolar DAC chip uses ADI (Analog Devices Inc.)'s LTC2664-12. The DAC chip has four output channels, one of which is used for actual measurement. If the DAC is 12 bits, the voltage resolution is:

$$\Delta V = \frac{(+5\mathrm{V}) - (-5\mathrm{V})}{2^{12}} \approx 2.44\mathrm{mV} \tag{5}$$

The voltage follower is implemented using TI (Texas Instrument)'s high output current amplifier LM7332, which can output a maximum current of up to 70mA, meeting design requirements.

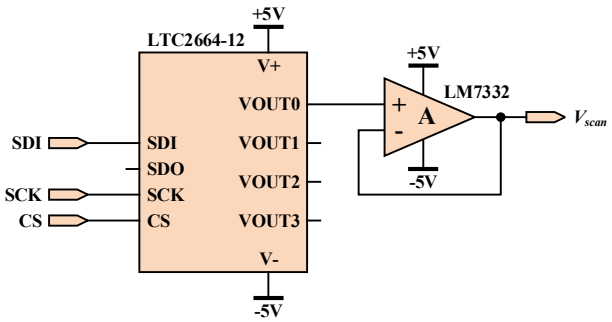


**Figure 4.** Schematic diagram of controllable voltage source circuit.

The dark current amplification circuit is shown in Figure 5, consisting of a cross-impedance amplifier (TIA), a programmable amplifier, and a general-purpose amplifier. TIA is realized by electrometer amplifier ADA4530-1 of ADI. This chip is an operational amplifier with an input bias current of flying ampere level, which is very suitable for measuring weak currents. The impedance connected in Figure 5 is 1MΩ, so the output voltage of TIA is:

Preprints (www.preprints.org) | NOT PEER-REVIEWED | Posted: 20 April 2023 doi:10.20944/preprints202304.0598.v1

$$V_1 = -R_1 I_{dark} \tag{6}$$

Due to the large range of dark current variation in PD detectors, especially in the case of reverse bias and forward bias, there is a greater difference in current. Therefore, a programmable amplifier is used to amplify $V_1$ to ensure a variable amplification factor. The programmable amplifier consists of ADI's instrument amplifier AD8220 and a single pole 8-position analog switch. The amplification factor of AD8220 is:

$$G = 1 + \frac{49.4\text{k}\Omega}{R_G} \tag{7}$$

The eight resistors connected to the single pole 8-position analog switch are 1MΩ, 12KΩ, 5.1KΩ, 1KΩ, 510Ω, 240Ω, 100Ω, and 51Ω, respectively. Based on the resistors $R_{x1}$~$R_{x8}$, the corresponding amplification factors can be calculated as 1.05, 5.22, 9.36, 50.40, 97.86, 206.83, 495.00, and 969.63. During testing, adjusting the amplification factor according to the size of the measured value can improve measurement accuracy, with A, B, and C being the address inputs of the analog switch, Controlled by the MCU.

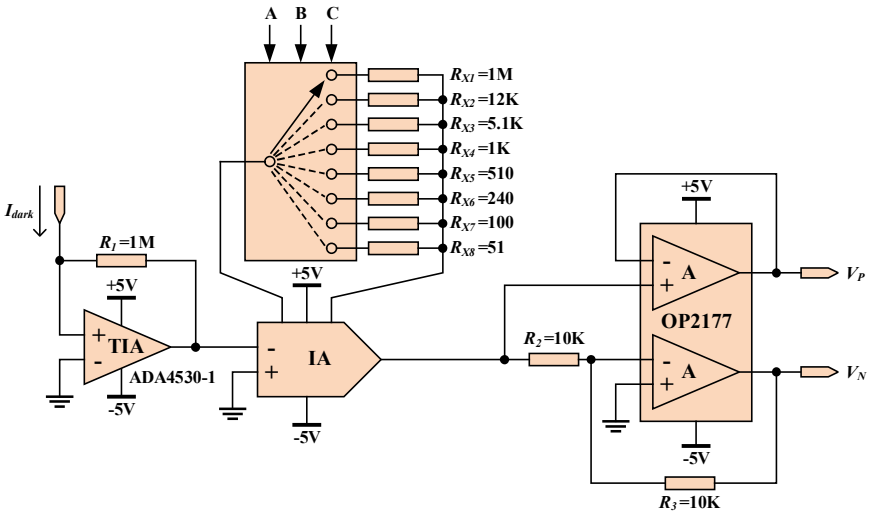


**Figure 5.** Dark current amplification circuit.

Due to the negative dark current of the PD detector under reverse bias and the positive dark current under forward bias, the value of $V_2$ can be either positive or negative, while the ADC inside the MCU can only read positive voltage. Therefore, we have designed a third-stage amplification circuit, which outputs in-phase voltage on one side and reverses voltage on the other side, namely:

$$\begin{cases} V_P = V_2 = -GR_1 I_{dark} \\ V_N = -V_2 = GR_1 I_{dark} \end{cases} \tag{8}$$

When $I_{dark}$<0, $V_P$>0, $V_N$<0, ADC reads the voltage of $V_P$; When $I_{dark}$>0, $V_P$<0, $V_N$>0, ADC reads the voltage of $V_N$; Use two ADC channels to read the $I_{dark}$ for reverse bias and forward bias respectively.

Using Toshiba Semiconductor's optical relay TLP3320 to achieve row and column selection of detector arrays, replacing mechanical relays with optical relays can reduce installation area and achieve fast switch selection. Figure 6(a) shows the internal structure of an optical relay, which is similar in principle to an optocoupler. The switching speed of TLP3320 is less than 300μs. Can achieve fast scanning of the array. The on-resistance of TLP3320 is about 10Ω, and the off-resistance is about $10^{14}$Ω. Usually, the dark current of the PD detector is between 1~100nA under a reverse bias voltage of 1V, and the equivalent resistance of PD is between $10^7$~$10^9$Ω. If the on-resistance $R_{ON}$ of TLP3320 is set to 10Ω, the off-resistance $R_{OFF}$ is set to $10^{14}$Ω, and the equivalent resistance $R_{PD}$ of PD is set to $10^8$Ω, the equivalent circuit of the array is shown in Figure 6(b). The on-current $I_{ON}$ is approximately $10^{13}$

Preprints (www.preprints.org) | NOT PEER-REVIEWED | Posted: 20 April 2023 doi:10.20944/preprints202304.0598.v1

times the off-current $I_{OFF}$, so the influence of the off resistance can be ignored. The dark current $I_A$ on the PD detector in the first row and column selected in Figure 6(b) is approximately equal to the dark current $I_{dark}$ of the array.

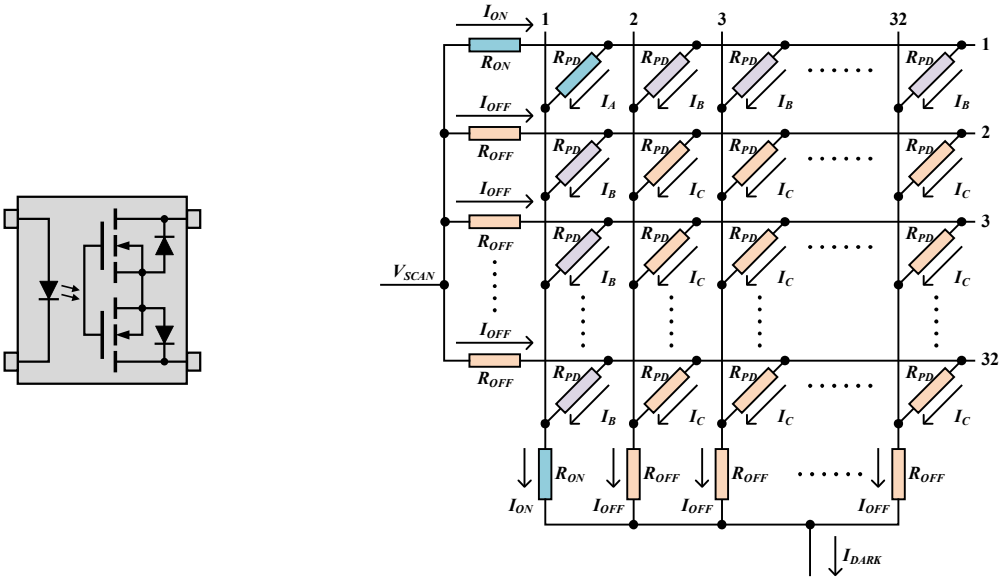


**Figure 6.** Optical relays and their equivalent circuits. (**a**) Internal structure of optical relays. (**b**) Equivalent scanning circuit.

As shown in Figure 7, the hardware diagram of the detection system is composed of a Ge-Si detector array and its scanning circuit, a variable voltage source, and dark current detection circuit, a control circuit, and an LCD display screen. The Ge-Si detector array is placed in the middle of the scanning circuit, and pixel selection is carried out by an optical relay. The variable voltage source and dark current detection circuit are integrated on a printed circuit board (PCB), and the bias voltage is output to the scanning circuit. The dark current is also connected to the dark current detection circuit from the scanning circuit. The control circuit is located below the LCD display screen, and the MCU used is the ARM chip STM32F103ZET6 from STMicroelectronics company. The LCD display screen can directly draw a bias voltage dark current curve and display the magnitude of dark current under different bias voltages. The system detection includes two modules: single measurement and continuous measurement. In the single measurement mode, rows and columns can be selected, and the bias voltage dark current curve of the row and column pixels can be measured in a single measurement; By continuously measuring the modulus, we can automatically measure the bias voltage dark current curve of all pixels at once, and ultimately store all test data in the SD card (Secure Digital Memory Card). By inserting the SD card into the computer host, we can read all data.

Preprints (www.preprints.org) | NOT PEER-REVIEWED | Posted: 20 April 2023 doi:10.20944/preprints202304.0598.v1

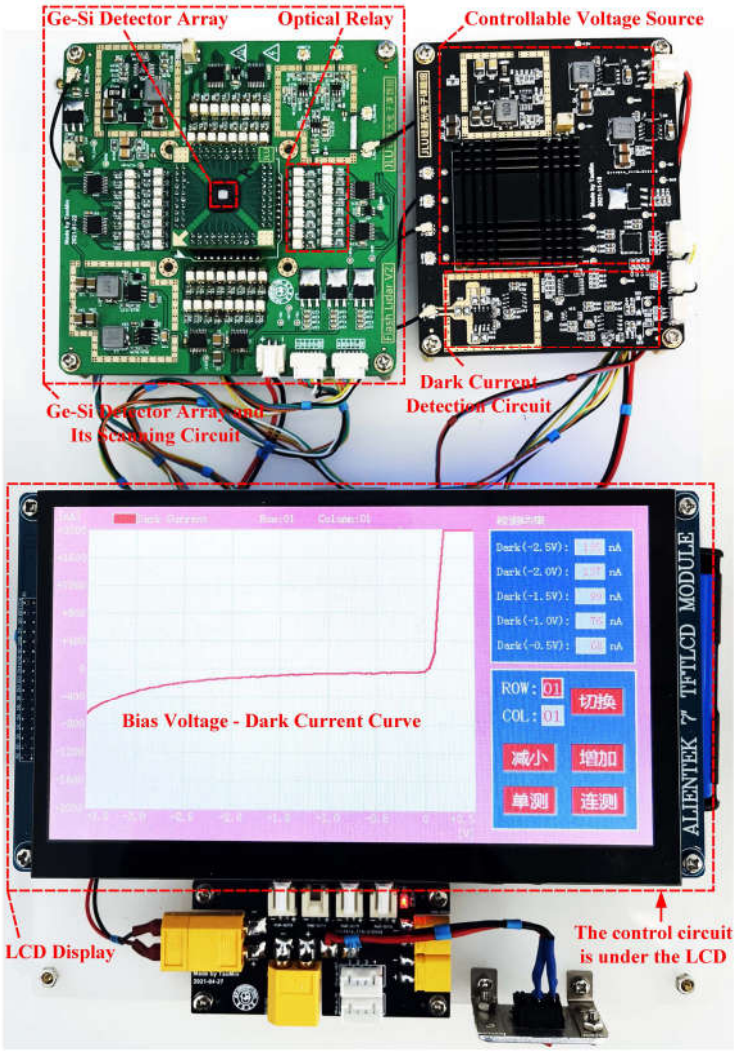


**Figure 7.** Hardware physical diagram of the detection system.

### 3. Array Test and Data Analysis

We have designed detector arrays of four different sizes, A, B, C, and D. The target surface of array A is 2.5cm×2.5cm, array B is 2.0cm×2.0cm, array C is 1.5cm×1.5cm, and array D is 1.0cm×1.0cm, as shown in Figure 8. We need to perform dark current detection on these four arrays and determine the distribution of dark current and pixel consistency under different sizes, ultimately guiding us in device design.

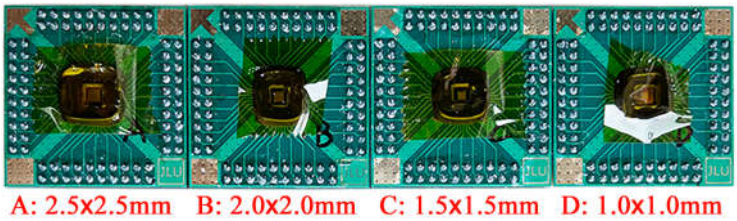


**Figure 8.** PD array chips (A, B, C and D).

Firstly, we measure the bias voltage dark current curve of a single pixel, as shown in Figure 9. The voltage scanning range is -350mV~+500mV, and the step voltage is 50mV. As shown in Figure 9, the bias voltage dark current curve of the first row and first column pixels of device A is completely consistent with the theoretical curve in Figure 2.

Preprints (www.preprints.org) | NOT PEER-REVIEWED | Posted: 20 April 2023 doi:10.20944/preprints202304.0598.v1

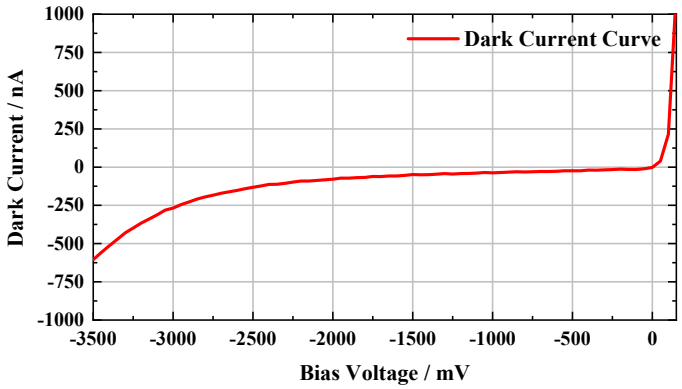


**Figure 9.** The bias voltage - dark current curve of the pixel.

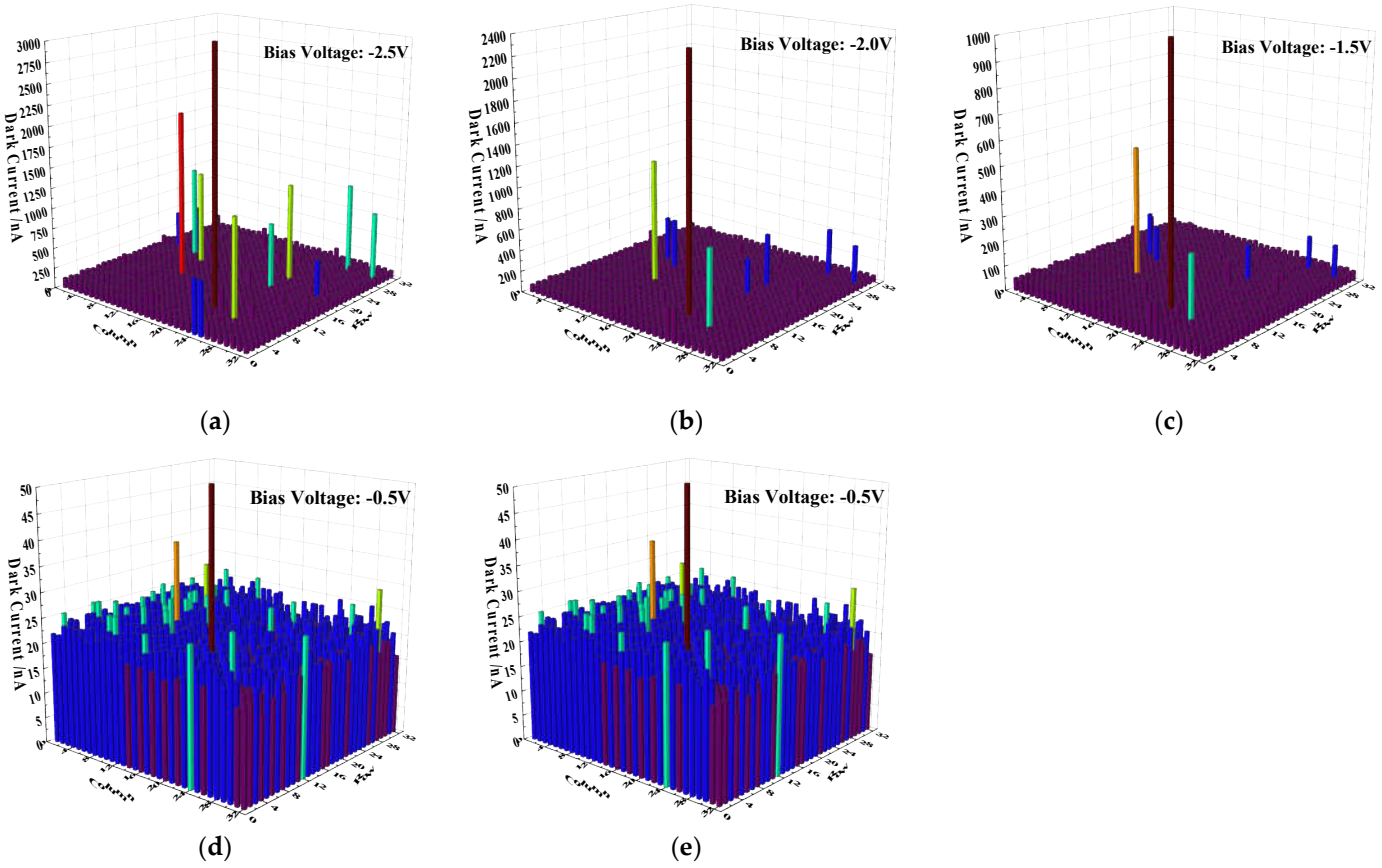


**Figure 10.** Histogram distribution of dark current test for PD array A. (**a**) Bias voltage=-2.5V. (**b**) Bias voltage=-2.0V. (**c**) Bias voltage=-1.5V. (**d**) Bias voltage=-1.0V. (**e**) Bias voltage=-0.5V.

Furthermore, we measure all dark currents in the device and determine their distribution characteristics. Figure 10 shows the two-dimensional histogram of the dark current distribution of device A, and Figure 10 shows the two-dimensional histogram of the dark current distribution at bias voltages of -2.5V, -2.0V, -1.5V, -1.0V, and -0.5V, respectively. The higher part of the histogram in the figure shows a large and abnormal dark current. To quantify the array damage, we counted the number of pixels greater than 10 times the average dark current and the number of pixels greater than 5 times the average dark current, respectively. Table 1 shows the measurement results. The number of pixels with device A greater than 10 times the average dark current is 2, with a total of 1024 pixels, accounting for 0.2%; The number of pixels with device A greater than 5 times the average dark current is 9, accounting for 0.9%. The pixel damage of device A is less than 1%, indicating good

Preprints (www.preprints.org) | NOT PEER-REVIEWED | Posted: 20 April 2023 doi:10.20944/preprints202304.0598.v1

performance. Our system can continuously detect device damage and quickly locate the position of damaged pixels, so we can respond to imaging applications through compensation in the later stage.

**Table 1.** PD array A's dark current parameters.

| Bias Voltage (V) | Average Dark Current (nA) | Number of Pixels Greater Than 10 Times the Average Dark Current | Number of Pixels Greater Than 5 Times the Average Dark Current |
|---|---|---|---|
| -2.5 | 147 | 2 | 9 |
| -2.0 | 86 | 2 | 7 |
| -1.5 | 54 | 2 | 3 |
| -1.0 | 35 | 0 | 2 |
| -0.5 | 22 | 0 | 0 |

Further, we measured the dark current and its distribution of devices A, B, C, and D, as shown in Table 2. According to the theoretical design, the smaller the pixel area, the smaller the average dark current. Figure 11(a) shows the average dark current values of devices A, B, C, and D when the bias voltages are -2.5V, -2.0V, -1.5V, -1.0V, and -0.5V, respectively. The higher the reverse bias voltage, the larger the average dark current. In theory, the average dark current is A > B > C > D. In actual measurements, A > B > C ≈ D is shown, and the pixel areas of devices C and D are not significantly different. All average dark currents are indistinguishable, The actual measurement is basically consistent with theoretical analysis.

**Table 2.** Distribution characteristics of dark current in PD arrays A, B, C, and D.

| Bias Voltage (V) | Average Dark Current (nA) | | | | Number of Pixels Greater Than 10 Times the Average Dark Current | | | | Number of Pixels Greater Than 5 Times the Average Dark Current | | | |
|---|---|---|---|---|---|---|---|---|---|---|---|---|
| | A | B | C | D | A | B | C | D | A | B | C | D |
| -2.5 | 147 | 75 | 28 | 24 | 2 | 10 | 4 | 3 | 9 | 11 | 8 | 5 |
| -2.0 | 86 | 47 | 15 | 15 | 2 | 7 | 1 | 0 | 7 | 11 | 6 | 5 |
| -1.5 | 54 | 27 | 8 | 12 | 2 | 5 | 1 | 0 | 3 | 8 | 4 | 1 |
| -1.0 | 35 | 16 | 5 | 9 | 0 | 4 | 1 | 0 | 2 | 5 | 2 | 0 |
| -0.5 | 22 | 9 | 2 | 8 | 0 | 1 | 0 | 0 | 0 | 1 | 5 | 0 |

Figures 11 (b) and (c) show the number of pixels with a bias voltage of -2.5V, -2.0V, -1.5V, -1.0V, and -0.5V for devices A, B, C, and D that are greater than 10 times the average dark current and 5 times the average dark current, respectively. All devices have a pixel damage rate of less than 1%, indicating good performance; Among them, device B has the most severe pixel damage and the worst performance, while device D has the least pixel damage and the best performance; The damage to devices A and C is relatively small, basically equivalent, and both have good performance. The above measurement results can guide us in the design of germanium silicon detector array chips. The detection system has good performance and can quickly detect the dark current characteristics of the device.

Preprints (www.preprints.org) | NOT PEER-REVIEWED | Posted: 20 April 2023 doi:10.20944/preprints202304.0598.v1

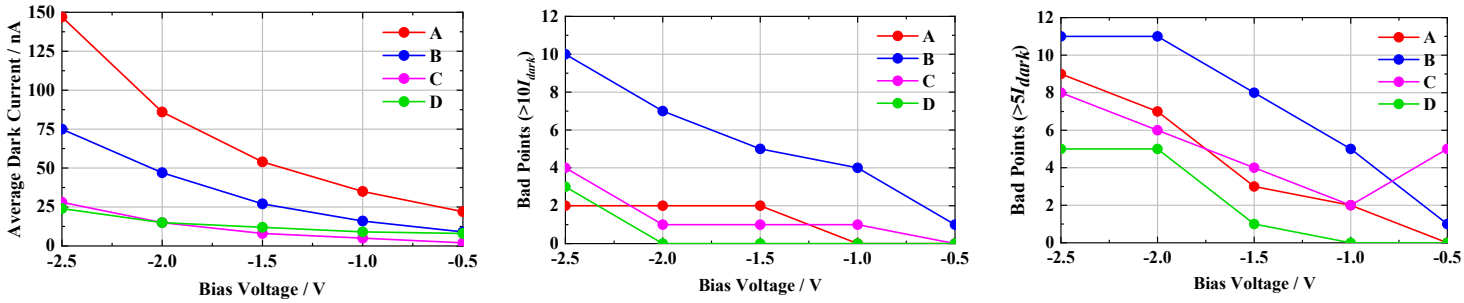


**Figure 11.** The distribution characteristics of dark current in PD arrays A, B, C, and D. (**a**) Average dark current distribution. (**b**) The distribution of the number of pixels greater than 10 times the average dark current. (**c**) The distribution of the number of pixels greater than 5 times the average dark current.

## 4. Conclusions

By analyzing the dark current characteristics and detection methods of Ge-Si photodetector arrays, this paper proposes and develops a dark current detection system for rapid scanning and detection of large-scale Ge-Si detector arrays. The high isolation optical relay is used to quickly select the pixels of the array chip, and the electrometer amplifier is used to amplify the dark current, so as to quickly detect the dark current of each pixel of the detector. We used this system to perform dark current detection on a series of array devices. The experimental results indicate that our designed system achieves rapid discrimination of array performance and rapid localization of damaged pixels. The scanning test results show that the average dark current of the detector array chip we designed is in the nano ampere level, and the proportion of bad points is less than 1%. The consistency of the array chip is high, which can meet the requirements of light detection at the receiving end of the LiDAR. This work laid the foundation for our subsequent development of a LiDAR prototype system.

**Author Contributions:** methodology, Z.G.; software, Z.G.; validation, X.L.; formal analysis, Z.L.; investigation, Z.W.; resources, C.L.; data curation, J.S.; writing—original draft preparation, Z.G.;writing—review and editing, M.T.; supervision, J.S.; project administration, M.T.; funding acquisition, J.S. All authors have read and agreed to the published version of the manuscript.

**Funding:** This research was funded by National Natural Science Foundation of China , grants number 62090053, 62090054 and 61934003; the Major Scientific and Technological Program of Jilin Province, grant number 20200501007GX; the Project of Industrial Technology Research and Development of Jilin Provincial Development and Reform Commission ,grant number 2020C019-2 and the Program for JLU Science and Technology Innovative Research Team, grant number 2021TD-39.

**Institutional Review Board Statement:** Not applicable.

**Informed Consent Statement:** Not applicable.

**Data Availability Statement:** The raw/processed data required to reproduce these findings cannot be shared at this time as the data also forms part of an ongoing study.

**Acknowledgments:** We are grateful to the anonymous reviewers for constructive comments that improved the quality of the work.

**Conflicts of Interest:** The authors declare no conflict of interest.

## References

1. F. Yang. Analysis of Lidar Technology Development Based on Autonomous Driving Competition[C]. International Conference of Optical Imaging and Measurement (ICOIM), Xi'an, China, 2021.
2. R. Roriz, J. Cabral and T. Gomes. Automotive LiDAR Technology: A Survey[J]. IEEE Transactions on Intelligent Transportation Systems, 2022, 23(7): 6282-6297.
3. L. Zhaohua and G. Bochao. Radar Sensors in Automatic Driving Cars[C], International Conference on Electromechanical Control Technology and Transportation (ICECTT), Nanchang, China, 2020.

4. Shan Y, Yao X, Lin H, et al. Lidar-Based Stable Navigable Region Detection for Unmanned Surface Vehicles[J]. IEEE Transactions on Instrumentation and Measurement, 2021, 70: 1-13.
5. Chiang K W, Tsai G J, Li Y H, et al. Development of LiDAR-Based UAV System for Environment Reconstruction[J]. IEEE Geoscience & Remote Sensing Letters, 2017, 14(10): 1790-1794.
6. Molebny V, Mcmanamon P, Steinvall O, et al. Laser radar: historical prospective—from the East to the West[J]. Optical Engineering, 2016, 56(3): 031220.
7. H. Månefjord, L. Müller, M. Li, et al. 3D-Printed Fluorescence Hyperspectral Lidar for Monitoring Tagged Insects[J]. IEEE Journal of Selected Topics in Quantum Electronics, 2022, 28(5): 1-9.
8. K. Sanjaya, F. Henning and K. R. Purba. 3D LIDAR City Model Application and Marketing Plan Development[C]. International Conference on Soft Computing, Intelligent System and Information Technology (ICSIIT), Denpasar, Indonesia, 2017.
9. D. Mongus and B. Žalik. Computationally Efficient Method for the Generation of a Digital Terrain Model From Airborne LiDAR Data Using Connected Operators[J]. IEEE Journal of Selected Topics in Applied Earth Observations and Remote Sensing, 2014, 7(1): 340-351.
10. J. Dai, X. Zhao, L. P. Li and X. F. Ma. GCD-YOLOv5: An Armored Target Recognition Algorithm in Complex Environments Based on Array Lidar[J]. IEEE Photonics Journal, 2022, 14(4): 1-11.
11. L. Singh, A. Srivastava and A. J. Sarkate. Thermal gradient effect on focus shift of laser & infrared optical assembly & thermal lensing by Nd-Yag laser rod in laser assembly of Optical Detection & Ranging System of Fighter Aircraft[C]. IEEE Uttar Pradesh Section International Conference on Electrical, Computer and Electronics (UPCON), Mathura, India, 2017.
12. G. Zhou, C. Li, D. Zhang, D. Liu, X. Zhou and J. Zhan. Overview of Underwater Transmission Characteristics of Oceanic LiDAR[J]. IEEE Journal of Selected Topics in Applied Earth Observations and Remote Sensing, 2021, 14: 8144-8159.
13. Hecht J. Laser instruments earn their place in space for communications and lidar[J]. Laser Focus World: The Magazine for the Photonics & Optoelectronics Industry, 2014.
14. Pham T, Wei D, Tran H, et al. Systematic study of Si-based GeSn photodiodes with 26m detector cutoff for short-wave infrared detection[J]. Optics Express, 2016, 24(5): 4519.
15. Batshev V I, Boritko S V, Kozlov A B, et al. Optical System of Visible and Short-Wave Infrared AOTF-based Spectral Imaging Device[C]. Wave Electronics and its Application in Information and Telecommunication Systems (WECONF). 2021.
16. Xu M, Wang J L, Chen T. Study on application of short wave infrared to detecting satellites in the daytime[J]. Optical Technique, 2008.
17. Ji, Sun, Chaowei, et al. Real-Time and High-Resolution Bioimaging with Bright Aggregation-Induced Emission Dots in Short-Wave Infrared Region[J]. Advanced Materials, 2018.
18. R. W. Millar et al. Ge-on-Si Single Photon Avalanche Diode Detectors for LIDAR in the Short Wave Infrared[C]. Conference on Lasers and Electro-Optics (CLEO), San Jose, CA, USA, 2020.
19. P. Vines, K. Kuzmenko, et al. High performance planar germanium-on-silicon single-photon avalanche diode detectors[J]. Nature Communications, 2019, 10: 1-9.
20. N. Duan, T. Y. Liow, A. E. J. Lim, et.al. 310 GHz gain-bandwidth product Ge/Si avalanche photodetector for 1550 nm light detection[J]. Opt. Express, 2012, 20(10): 11031.
21. Y. M. Kang, H. D. Liu, M. Morse, et.al. Monolithic germanium/silicon avalanche photodiodes with 340 GHz gain–bandwidth product[J]. Nature Photonics, 2009, 3: 59–63.
22. L. Virot, P. Crozat, J.-. Fédéli, et.al. Germanium avalanche receiver for low power interconnects[J]. Nature Communications, 2014, 5: 4957.
23. R. E. Warburton, G. Intermite, M. Myronov, et.al. Ge-on-Si Single-Photon Avalanche Diode Detectors: Design, Modeling, Fabrication, and Characterization at Wavelengths 1310 and 1550 nm[J]. IEEE Transactions on Electron Devices, 2013, 60(11): 3807-3813.
24. N. J. D. Martinez, M. Gehl, C. T. Derose, et.al. Single photon detection in a waveguide-coupled Ge-on-Si lateral avalanche photodiode[J]. Optics Express, 2017, 25: 16130-16139.
25. Y. Li, X.-S. Luo, G. Liang, et.al. Demonstration of Ge/Si Avalanche Photodetector Arrays for Lidar Application[J]. OFC, Tu3E.3.pdf , 2019.
26. Dong-Liang, Zhang, Bu-Wen, et al. Theoretical study of the optical gain characteristics of a Ge1xSnx alloy for a short-wave infrared laser[J]. Chinese Physics B, 2015(2):7.
27. Cai Zhimeng, Chen Liqun, Li Cheng. Characteristics of SOI - based RCE - Ge photodetectors[J]. Journal of Fuzhou University, 2016, 44(5): 656.
28. J. Cui and Z. Zhou. High-performance Ge-on-Si photodetector with optimized DBR location[J]. Optics Letters, 2017, 42(24): 5141-5144.
29. Hui Zhang, Chenghu Ke, Zhaohui Liu. Modeling and simulation analysis of PIN photodetector[J]. Journal of Applied Optics, 2019, 40(5): 723-730.
30. Jun Zhao, Research on Photodetector equivalent circuit model and experiment[D]. Chongqing University, 2015.